Journal of Power Sources 369 (2017) 111–121

Contents lists available at ScienceDirect

Journal of Power Sources

journal homepage: www.elsevier.com/locate/jpowsour

Microstructural stability of supported metal catalysts: A phase field approach

Ryan Davis [a], Mikko Haataja [a, b, c, *]

[a] Department of Mechanical and Aerospace Engineering, Princeton University, Princeton, NJ 08544, USA
[b] Princeton Institute for the Science and Technology of Materials (PRISM), Princeton University, Princeton, NJ 08544, USA
[c] Program in Applied and Computational Mathematics (PACM), Princeton University, Princeton, NJ 08544, USA

HIGHLIGHTS

- Simulation study of microstructural stability of infiltrated metal catalysts.
- Maximum total triple phase boundary density near 4–7% infiltration loading.
- Catalyst deactivation by Ostwald ripening and particle migration/coalescence.

ARTICLE INFO

Article history:
Received 23 July 2017
Received in revised form
14 September 2017
Accepted 20 September 2017

Keywords:
SOFC
Infiltration
Catalyst
Phase field
Triple phase boundary
Sintering

ABSTRACT

The long-term stability of supported metal catalysts designed for solid-oxide fuel cell (SOFC) anodes is evaluated using a phase field simulation approach. Porous support structures are numerically sintered and then infiltrated with a nanoscale catalyst phase to mimic scaffolds fabricated via both pyrolysis and acid leaching techniques. Simulations capture the dewetting, particle agglomeration, and coarsening processes that occur during extended operation at elevated temperatures. We systematically explore the microstructural evolution of the active phase for a range of infiltration loadings from 2 to 21% and report on common performance metrics, such as triple phase boundary (TPB) density and contiguity. Ostwald ripening and particle migration and coalescence events are identified as dominant mechanisms contributing to severe reductions in the TPB density and catalyst deactivation. Despite marked differences between the simulated pyrolyzed and leached scaffold structures, the resulting TPB densities are comparable in value. Additionally, we show that tuning the metal catalyst/scaffold contact angle between 60° and 120° does not significantly affect TPB density. More broadly, this work elucidates the challenges associated with stabilizing nanoscale dispersions prepared by infiltration and similar techniques.

1. Introduction

Supported metal catalysts comprise an important class of structures within heterogeneous catalysis that have many applications from hydrocarbon transformation to environmental protection. They are characterized by a large, porous support structure and a catalytically active metal as a minority phase. The immense surface area of the porous support enables the active phase to be dispersed on the surface in the form of small particles or a semi-continuous layer to achieve high catalytic activity. Supported catalysts can be fabricated using a number of techniques to disperse the active phase onto the support. These include infiltration, precipitation, ion-exchange, and others [1]. Despite the many details of these variations, the result of a highly active and stable supported catalyst is a common objective.

Supported metal catalysts have become a promising approach to the design of electrodes for solid-oxide fuel cells (SOFCs). The fabrication technique typically used in this application is infiltration, particularly wet-chemical impregnation [2]. The process has been shown to alleviate many of the degradation issues that hinder the commercialization of SOFC technology. This is attributed to the numerous advantages it has over conventional methods in delivering microstructures that are engineered at both nano and microscopic length scales [3]. The introduction of infiltration to create supported catalyst electrodes has opened many questions

* Corresponding author. Department of Mechanical and Aerospace Engineering, Princeton University, Princeton, NJ 08544, USA.
E-mail address: mhaataja@princeton.edu (M. Haataja).

https://doi.org/10.1016/j.jpowsour.2017.09.066
0378-7753/

regarding the unique requirements and optimizations of SOFC structures, especially in terms of long-term stability [4]. In this work, we focus on the particular application of infiltration to fuel cell technology to study the microstructural stability of supported metal catalysts. We address many of the questions involving fuel cell optimization and offer insight into the catalyst evolution using a continuum simulation approach.

The conventional nickel(Ni)-based cermet anode is fabricated by co-sintering nickel-oxide (NiO) particles with particles of an ionically conducting phase, usually yttria-stabilized zirconia (YSZ), and reducing the NiO to Ni. However, the performance of these anodes suffers dramatically from degradation mechanisms such as metallic-phase coarsening and redox fracture [5]. Alternatively, a mixed-ionic-electronic-conducting (MIEC) material can be used to combine the electronic and ionic pathways, simplify the microstructural requirements, and improve stability. Unfortunately, MIECs alone do not provide ample catalytic activity or bulk conductivity and often require an additional catalyst [5]. Infiltration may improve the stability of Ni-based YSZ cermets or enhance the catalytic activity of MIEC structures. Although it is applicable to both anode and cathode construction, in this work, we focus on anode structures.

The general approach of the infiltration technique is to construct a highly porous backbone as the primary structure, subsequently infiltrate the secondary components via aqueous salt solution, and decompose the infiltrated solution. The desired result is a large-scale porous backbone structure, known as the scaffold, whose surface is decorated with a nano-scale layer of the active phase. Typically, the scaffold provides the structural integrity and ionic conductivity while the infiltrated material serves as the catalyst and electron conductor. The advantages of this technique are numerous. Firstly, the piece-wise nature of the construction process allows the low-melting point infiltrate material to bypass the sintering stage of the high-melting point backbone material, avoiding undesirable coarsening, melting, or solid-state reactions. Additionally, the uniform distribution of nanoscale catalyst particles leads to a significant boost in electrochemical activity as well as mechanical stability against expansion of the metal phase during oxidation [3]. Furthermore, infiltration has proven its flexibility in the wide array of material selections that have been tested for both the cathode and anode. This enables the use of alloyed catalyst to reduce coke formation and sulfur poisoning [5]. The most significant drawback of the technique is the time intensive process of infiltrating the solution, which usually requires multiple iterations. However, progress on this front is being made through modifications such as vacuum assistance, solution additives, molten salt solution, and pretreated scaffold surfaces [4,6].

A primary concern for infiltrated systems is the amount of infiltrated material required to form a percolating or semi-continuous network. This is particularly true for scaffolds with purely ionic conductivity because the infiltrated material must serve as the conduit for electron transport. Experimental studies are unclear on the required infiltrate loading, especially after extended operation. Sufficient conductivity has been measured experimentally shortly after fabrication at various infiltration loadings of 10% [7], 12% [8], and 14% [9]. However, each of these cited studies observe degradation and note the possibility of particle agglomeration during extended usage. Using three-dimensional imaging techniques, Kishimoto et al. find that there is no percolating cluster in a Ni-infiltrated anode with 20% infiltration loading after decomposing the precursor solution at 500 °C [10]. It seems that stabilizing a contiguous network at elevated temperatures may be formidable, and this issue calls for a systematic analysis of the long-term stability of these structures.

Another important requirement is ensuring sufficient triple phase boundary (TPB), a metric often correlated with catalytic activity [2]. Theoretical and numerical models have provided significant insight on this front. Using a two-dimensional lattice percolation model, Hardjo et al. demonstrated that the TPB goes through a maximum at infiltration loadings around 15% [11]. This work was followed by a series of numerical studies that use particle placement algorithms to procedurally generate infiltrated systems on three-dimensional discretized grids from which microstructural properties can be calculated [12–14]. Of note are the results of Zhang et al. that show percolation thresholds between 4 and 10% and maximal TPB values around 8–15%, depending on factors such as porosity and particle size ratio [12]. Their model was extended using a kinetic Monte Carlo (kMC) approach to study the thermodynamic evolution of infiltrated particles on short ($\sim 1s$) timescales, and the pairwise interaction parameter was varied to effectively set the phase wettability [15]. It has also been demonstrated that a phase field approach can be applied to infiltrated systems [16]. To summarize the study, three infiltration loadings of 1%, 1.6%, and 2.2% were tested on a 60^3 grid system for a single scaffold, and a maximum TPB was reported at 1.6% loading. In the present work, the phase field method is employed to provide deeper insight into the long-term stability of these structures with a closer examination of phase connectivity, the properties of scaffold structures, and a wide range of infiltration loadings. Specifically, we wish to expound on these ideas with a systematic study over the range of 2%–20% infiltration loading for multiple scaffold morphologies at a spatial resolution that can resolve the disparity in particle sizes while allowing for extended time evolution. In contrast to the kMC method, the phase field model parameters can be readily converted to interfacial energies in order to perform a parametric study across a wide range of contact angles.

In this work, we perform a systematic study of the long-term stability of infiltrated systems and analyze microstructural evolution due to particle agglomeration and coarsening. A phase field formulation is developed to handle scaffold sintering and to simulate the evolution of the active phase that is driven by capillary forces. We report that these supported metal catalyst systems show a significant enhancement in TPB at early times, in agreement with previous studies. However, continual degradation takes place through particle sintering and coarsening, which ultimately removes the advantages of a nanoscale dispersion. We identify particle migration and Ostwald ripening as mechanisms that cause particle growth in systems with low active phase loading. A quantitative analysis of particle size evolution reveals scaling behavior consistent with kinetics dominated by particle migration. The active phase contiguity undergoes significant losses due to instabilities in the semi-continuous infiltrate network. We investigate scaffolds of different morphologies that are produced using acid leaching and pyrolysis to remove pore-former particles. Additionally, we explore the effect of phase interaction and contact angle by altering the surface energetics of the active phase.

2. Continuum approach

The phase field modeling technique is a powerful tool to study the spatio-temporal evolution of multiphase systems driven by a reduction in the free energy of the system [17]. By employing an implicit representation of diffuse interfaces, complex microstructural reorganization processes such as particle merging and ligament splitting can be handled naturally without explicitly tracking the interface. We utilize a phase field approach to directly simulate two processes in this study: the long-term coarsening of the infiltrated catalyst phase and the polycrystalline particle sintering during scaffold construction. Two different models are developed for these two processes in order to capture the specific physics

involved in each. This section is divided into three parts. First, the phase field model for infiltrate coarsening is presented in Sec. 2.1, and the model parameters are connected to physical properties. In Sec. 2.2, the model is extended to include particle sintering. Finally, the steps involved in the scaffold construction process are detailed in Sec. 2.3.

2.1. Phase-field coarsening model

To study the evolution of an infiltrated catalyst phase, we use a multi-phase field model. Three order parameters are introduced to represent the scaffold (ϕ_1), active catalyst (ϕ_2), and pore (ϕ_3) phases. For clarification, the term "active catalyst phase" refers to the infiltrated material in its final stage of infiltration, after intermediate processing steps of drying, calcination, and reduction. It is considered here to be metal, such as Ni, and may also be referred to as the infiltrate or catalyst phase. Each of the order parameters takes a value of 1 in the bulk of its respective phase, a value of 0 outside, and varies continuously across the interface. The free energy functional is given as

$$F_\phi = \int_V \left\{ \sum_{i=1}^{3} \left[A_i f(\phi_i) + \frac{W_i}{2} \left| \nabla \phi_i \right|^2 \right] + C \left[\phi_1^2 \phi_2^2 + \phi_1^2 \phi_3^2 + \phi_2^2 \phi_3^2 + \prod_{i=1}^{3} (1-\phi_i)^2 \right] \right\} d\mathbf{r}, \tag{1}$$

where i serves as an order parameter index. Each order parameter is assigned a standard double-well potential, $f(\phi) = \phi^2(1-\phi)^2$, and a squared-gradient term, where A_i and W_i are model parameters. In addition, a obstacle potential with strength C is included to penalize the formation of overlapping order parameters or unphysical phases. The order parameters are evolved with conservative kinetics described by the Cahn-Hilliard equation

$$\frac{\partial \phi_i}{\partial t} = \nabla \cdot \left[M(\phi_i) \nabla \frac{\delta F_\phi}{\delta \phi_i} \right], \quad i \in \{1,2,3\}, \tag{2}$$

where M is related to the atomic mobility. The mobility of the solid phases can be limited to the interface by formulating it in terms of the order parameter as $M(\phi_i) = M_i \tanh(\left|\nabla \phi_i\right|^2/\xi)$, where ξ sets the width of the mobility region around the interface. The mobility of the pore phase is set to be constant, $M(\phi_3) = M_3 = 1.0$.

The model can be made nondimensional with the introduction of a characteristic time scale (τ), length scale (Δx), and reference energy (E). For convenience, we also introduce the dimensionless quantities $\overline{M} = \tau M E/\Delta x^2$, $\overline{A_i} = A_i \Delta x^3/E$, and $\overline{W_i} = W_i \Delta x/E$ so that the nondimensional equations appear as the dimensional ones (Eqns. (1) and (2)) but with dimensionless quantities. Using the relation $M = D_s/(\partial \mu/\partial \phi)|_{eq}$, the characteristic time can be expressed as $\tau = 16\overline{W}\Delta x^4/D_s\delta^2$, where D_s is the surface diffusivity of the infiltrate. We take Δx to be the grid spacing and choose $\Delta x = 15\ nm$ such that scaffold particles are about 1 μm, typical of experimental systems. The surface diffusivity can vary several orders of magnitude depending on the operation temperature. Taking the surface diffusivity to correspond with that of Ni as estimated from sintering data at temperatures down to 600°C gives $D_s \approx 10^{-12} m^2/s$ [18]. The physical interface width is estimated to be $\delta \approx 1 nm$. With these values, the characteristic time is $\tau \approx 2s$, making our simulations with 10^7 times steps and step size $\Delta t = 0.002\tau$ correspond to approximately 10 h of real time.

The free energy in Eq. (1) incorporates three order parameters and employs seven model parameters: A_1, A_2, A_3, W_1, W_2, W_3, C. For the purpose of parameterizing the model, we seek to establish a connection between the model parameters and the physical properties of the system. To this end, three interface energies, γ_{12}, γ_{13}, and γ_{23} are associated with the three interfaces in the system, and each interface is constrained to feature a constant numerical interface width, δ. Following the procedures presented in Ref. [19], the order parameter profiles are matched at the interface and the physical properties are formulated in terms of model parameters. We have tailored the free energy functional in Eq. (1) such that this matching procedure can be carried out for a range of surface energy values. As a result, the parameters must satisfy two constraint equations, $W_1 / W_2 = (A_1 + C) / (A_2 + C)$ and $W_1 / W_3 = (A_1 + C) / (A_3 + C)$, in order to maintain a constant interface width. The surface energies can be expressed as $\gamma_{ij} = 2(W_i + W_j) / 3\delta$ for γ_{12}, γ_{13}, and γ_{23}. Lastly, the constant interface width takes the form $\delta = 4\sqrt{(W_1 + W_2)/2(A_1 + A_2 + 2C)}$. This approach to parameterization gives six equations relating the seven model parameters to physical properties, which allows some freedom in setting the strength of the obstacle potential.

The values of the model parameters can now be chosen to satisfy the two constraint equations, as well as produce the desired interface energies and interface width. In order to perform a parametric study on the effect of phase wettability, the surface energies are chosen in order to produce a desired equilibrium contact angle, θ_c, between the infiltrate and scaffold. Using Young's balance for an infiltrate particle on a scaffold substrate, $\gamma_{12} + \gamma_{23} \cos\theta_c = \gamma_{13}$, the contact angle can be expressed in terms of model parameters as

$$\theta_c = \arccos \sqrt{\frac{(W_1 + W_3)^2 - (W_1 + W_2)^2}{(W_2 + W_3)^2}}. \tag{3}$$

With the set of equations discussed here, three sets of parameters are generated to correspond to three contact angle $\theta_c = 60, 90, 120°$. Table 1 summarizes the physical properties and the model parameters used in this work. While the range of contact angles is chosen to facilitate a parametric study for generic infiltrate and scaffold materials, we note that the equilibrium contact angle for Ni particles on a YSZ substrate is estimated experimentally to be approximately 117 ° [20].

During coarsening, the scaffold phase is assumed to be static, $M_1 = 0.0$, while the interface mobility of the infiltrated catalyst is set to unity, $M_2 = 1.0$. For an Ni-infiltrated YSZ anode, assuming that the scaffold is static is reasonable given that the surface diffusivity of zirconium ions on a YSZ surface is estimated from sintering data to be around $10^{-18} m^2/s$ at 900 ° C [21], nearly 7 orders of magnitude slower than that of Ni surface self-diffusion [18]. We choose ξ such that the width of the mobility region is comparable to the interface width. For the choice $\xi = 0.036$, the full width at half maximum of the mobility region is equal to the numerical interface width $\delta = 3\Delta x$. It is important to note that the active phase mobility can take small, yet finite, values outside of the mobility region. This is especially true near the support surface where it is found to be 0.001 relative to its maximum value. Over the course of extended

Table 1
The values of the nondimensional physical and model parameters used in this study to achieve contact angles $\theta_c = 60°, 90°, 120°$ between the infiltrate and scaffold phases.

θ_c(°)	δ	γ_{13}	γ_{23}	γ_{12}	A_1	A_2	A_3	C	W_1	W_2	W_3
60	3.0	1.0	1.0	0.5	0.3	0.3	2.3	0.7	1.125	1.125	3.375
90	3.0	1.0	1.0	1.0	1.0	1.0	1.0	1.0	2.250	2.250	2.250
120	3.0	1.0	2.0	2.0	0.5	4.5	0.5	1.5	2.250	6.750	2.250

coarsening, this small mobility can have significant consequences and is discussed further in Sec. 3.

2.2. Phase-field sintering model

The model given in Sec. 2.1 for coarsening can be extended to represent the polycrystallinity of the solid phases with multiple grain orientations. This is used to model the sintering process of scaffold construction. In this case, the three order parameters represent the scaffold particles (ϕ_1), pore-former particles (ϕ_2), and pore space (ϕ_3). A finite number of grain orientations are represented with the set of order parameters η_{1i} for the scaffold phase and with η_{2j} for the pore-former particles. The indices, i and j, vary from 1 up to the number of grains in the set for each phase. Each set of grain orientations is coupled to its parent phase through a component of the free energy,

$$F_{\eta_i} = \int_V \sum_j \left[B_i f\left(\eta_{ij}\right) + \frac{\kappa_i}{2} \left| \nabla \eta_{ij} \right|^2 \right] d\mathbf{r} + \int_V D_i \left((1-\phi_i)^2 \sum_j \eta_{ij}^2 + \phi_i^2 \sum_{j<k} \eta_{ij}^2 \eta_{ik}^2 + \phi_i \prod_j \left(1-\eta_{ij}\right)^2 \right) d\mathbf{r}. \tag{4}$$

Similar to above, each grain orientation, η_{ij}, is assigned a standard double-well potential $f(\eta) = \eta^2(1-\eta^2)$ and squared-gradient term with parameters B_i and κ_i. An obstacle potential of strength D_i couples the η_{ij} parameter to its parent phase, ϕ_i, and prevents overlap between the grains. The total free energy of the system containing three phases, two of which have multiple grain orientations, can be expressed as $F = F_\phi + F_{\eta_1} + F_{\eta_2}$. The solid phases are evolved using conserved kinetics described by the Cahn-Hilliard equation with the appropriate free energy components,

$$\frac{\partial \phi_i}{\partial t} = \nabla \cdot \left[M(\phi_i) \nabla \frac{\delta \left(F_\phi + F_{\eta_i}\right)}{\delta \phi_i} \right] \tag{5}$$

The grain orientation parameters are evolved using non-conserved kinetics described by the Allen-Cahn equation,

$$\frac{\partial \eta_{ij}}{\partial t} = -L \left(\frac{\delta F_{\eta_i}}{\delta \eta_{ij}} \right) \tag{6}$$

The mobility of the solid phases is limited to the interface using the form $M(\phi_i) = M_i \tanh(\left|\nabla \phi_i\right|^2 / \xi)$ where M_i sets the maximum mobility and ξ sets the width of the mobility region.

The values of the model parameters used during the sintering stage of scaffold construction are listed as follows: $A_1 = 0.2$; $A_2 = 0.2$; $A_3 = 0.6$; $B_1 = 1.6$; $B_2 = 1.6$; $C = D_1 = D_2 = 0.4$; $W_1 = W_2 = W_3 = 1.125$; $\kappa_1 = \kappa_2 = 2.25$. This set of parameters gives a 120° contact angle of pore-former particles on scaffold surfaces and a 120° dihedral angle at the triple junction between two grains and pore space. For scaffold and pore-former particles present during sintering, the interface mobility is set to $M_1 = M_2 = 1.0$ and $\xi = 0.036$. The mobility of the grain orientation parameters is taken to be $L = 1.0$. Sintering simulations are run for 10^6 time steps with $\Delta t = 0.002\tau$.

The numerical simulation of both particle sintering and active phase coarsening models are carried out using finite differencing techniques. The simulation domain is discretized as a uniform, rectangular grid of 180^3 points. Parallelization is implemented with OpenMPI using a multidimensional domain decomposition and typically executed using 16 processors and 72 h per simulation. The Laplacian operator is evaluated with a 7 point stencil, and the equations of motion are integrated using an explicit forward-Euler scheme. These techniques are standard within the phase field community [22], and simulations are numerically stable for time steps employed in the present work.

2.3. Scaffold structure generation

The supported metal catalyst systems used in this study are constructed through a multistep process designed to emulate the fabrication and operation procedures typical of SOFC technology. The scaffold structure must be sufficiently porous to ensure adequate transport of a gaseous fuel. Experimentally, the porosity is controlled by mixing sacrificial pore-former particles with the scaffold particles during fabrication of the support. The pore-former particles are later removed, leaving behind porous space. There are two techniques commonly used to remove the pore-former particles: pyrolysis and acid leaching [5]. In pyrolysis, pore-former particles of graphite, starch, or polymer are removed early during the sintering stage through melting or combustion. In acid leaching, oxide particles (typically NiO) remain intact during the sintering stage and can be selectively removed after sintering by reduction and an acid wash [5].

Fig. 1 shows the step-by-step construction of scaffolds representative of acid leaching (a) and pyrolysis (b). For all scaffolds, construction begins by seeding 30 particle centers with a random, periodic, hard-sphere packing in three dimensions [23]. This produces large-scale particles with radius around $0.17L$, where L is the linear system size. The particles are randomly labeled as scaffold (shown as grey) or pore-former (shown as orange) particles to establish a 50:50 solid volume ratio. To account for the polycrystalline nature of the particle packing, each of the particles is assigned one of a finite number of grain orientations, represented in Fig. 1 as different shades of color. These are assigned using a graph coloring algorithm so that no two neighboring particles of like-type share the same grain orientation. Neighbor pairs are determined by the face-sharing cells of a periodic Voronoi tessellation [24]. The particle radius is then enlarged to account for the densification that takes place during sintering. To mimic acid leaching, scaffold particles are expanded until a dense system is obtained [Fig. 1(a)]. For pyrolysis scaffolds, the radius is extended to $0.2L$ resulting in a lens of overlapping region between adjacent particles [Fig. 1(b)].

The systems are sintered using the phase field model developed above for polycrystalline sintering. In addition to establishing smooth and diffuse interfaces, the sintering process produces more realistic scaffold features such as faceted faces, rounded edges, and the desired dihedral angle. To match the pyrolysis process, pore-forming particles are removed *before* sintering. Alternatively, for the acid leaching process, pore-forming particles are removed *after* sintering. These two processes produce strikingly different microstructural support features as illustrated in Fig. 1 and discussed further in Sec. 3. Application of the active, or catalyst, material is carried out by inserting the secondary phase as a coating on the surface of the sintered scaffold. The thickness of this uniform layer is chosen to produce the desired volume fraction. Numerically, this is accomplished by establishing a signed distance function from the scaffold surface and filling all of the grid points within the appropriate distance. Finally, after particle packing, scaffold sintering, and infiltration, the active phase can be evolved using the phase field model developed above for coarsening.

3. Results

3.1. Microstructural evolution of infiltrate

After infiltration, the microstructure of the catalyst phase is

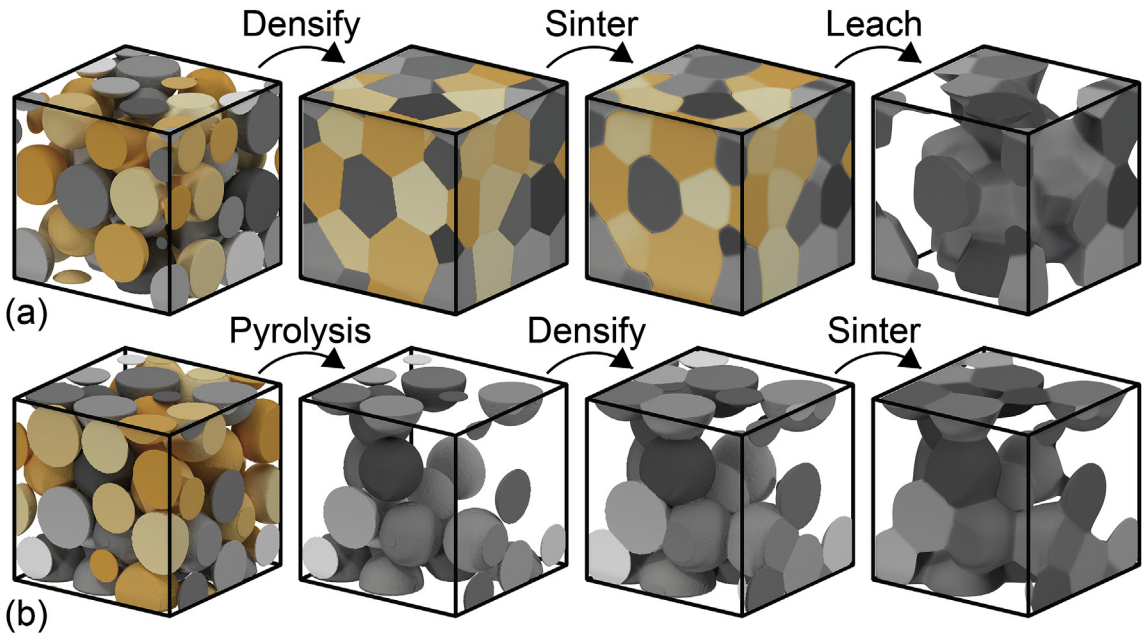

Fig. 1. Numerical scaffold construction is a multistep process involving scaffold (grey) and pore-former (orange) particles. The top row (a) illustrates the process for leaching pore-former particles after sintering while the bottom row (b) shows pyrolysis before sintering. (For interpretation of the references to colour in this figure legend, the reader is referred to the web version of this article.)

suspected to evolve while subject to elevated temperatures, as is the case for SOFC anodes. The processes involved in this evolution are illustrated in Fig. 2 with a sequence of representative configurations. The system is composed of 50% scaffold material, by volume, and the pores are formed by leaching sacrificial particles after sintering. The volumetric fraction of the catalyst phase, referred to as the infiltration loading, is 7%, and its equilibrium contact angle with the scaffold is $\theta_c = 120^\circ$. The infiltrate is initialized as a continuous layer on the scaffold surface, as shown in Fig. 2(a). In the early stages of evolution, the infiltrate layer dewets the surface due to strong geometric heterogeneities. It is well known that a uniform film on a planar substrate is in a metastable state and will dewet the surface given a preexisting hole in the film [25]. While a flat film surface is stable against small perturbations, hole formation is possible through heterogeneities in the film or substrate. Early in the agglomeration process, the infiltrate phase exhibits a semi-continuous network of cylindrical ligaments and isolated clusters [Fig. 2(b)]. Visual inspection reveals that the ligaments undergo Rayleigh-type splitting events [26], and a distribution of particles with similar sizes and separation distances emerges on the surface [Fig. 2(c)]. Although the rate of coarsening slows at later times, the particles continue to become larger and more isolated [Fig. 2(d)]. The triple phase boundary, as indicated by the black line at the surface intersections, undergoes notable evolution during the dewetting and coarsening processes.

Using the same scaffold, the initial layer thickness of the active phase is altered to achieve eight different infiltration loadings between 2% and 21%. The final configurations ($t = 20000\tau$) after evolution are displayed in Fig. 3 for each loading. As expected, the loading has a significant impact on the active phase microstructure. For the lowest loadings (2 and 4%), we observe a dispersion of small particles form rapidly on the scaffold surface at early times and continue coarsening throughout the simulation. The active phase particles tend to localize along the grain boundaries and particle junctions of the scaffold. At intermediate loadings, similar behavior is observed except that the particle sizes are much larger. After coarsening, the active phase particles are comparable in size to the scaffold particles as shown in Fig. 3(c–f) for loadings 7, 9, 11, and 14%. As the particle size increases, the scaffold heterogeneity plays a larger role as evidenced by the highly non-spherical shape of the active phase particles. At the largest loadings, 18 and 21%, the active phase requires a lengthy amount of time to dewet the surface. After

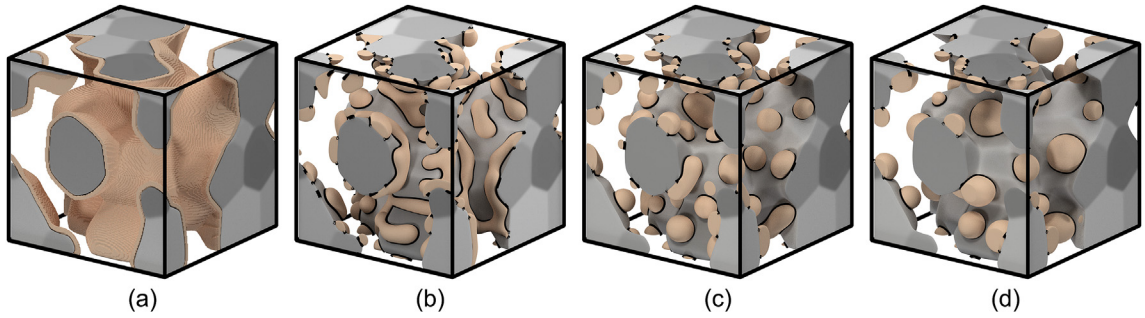

Fig. 2. A sequence of configurations shows the active phase (orange) dewetting and coarsening on the scaffold surface (grey) for 7% infiltration loading. The snapshots are taken at times $t =$ (a) 0, (b) 1, (c) 5, and (d) $20 \times 10^3\tau$ and the TPB is traced by black lines at the phase intersections. (For interpretation of the references to colour in this figure legend, the reader is referred to the web version of this article.)

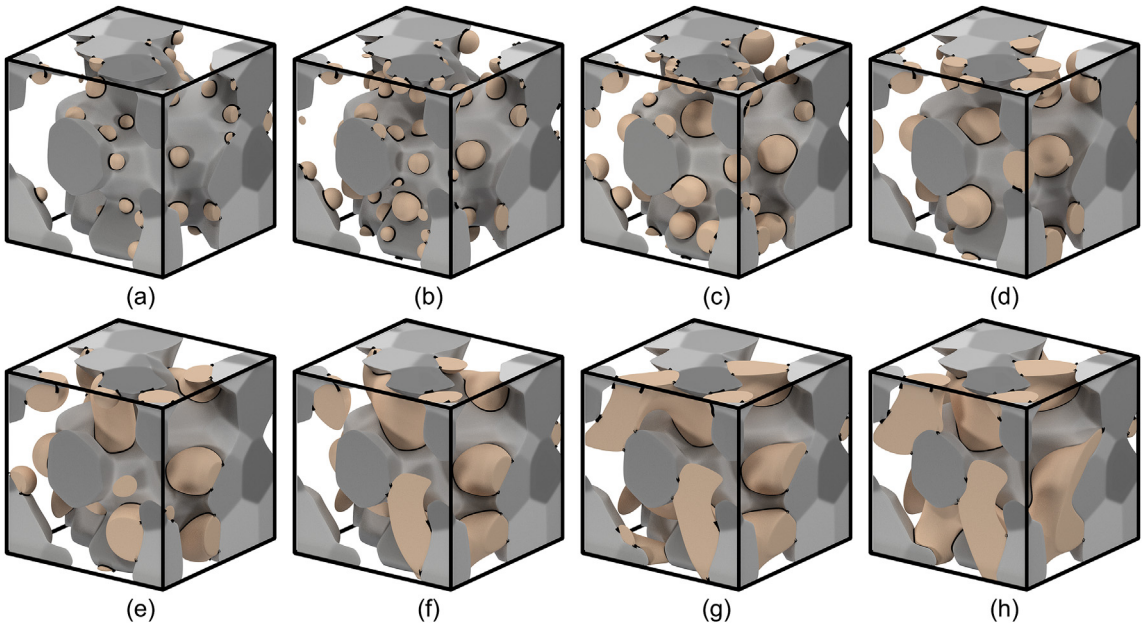

Fig. 3. Final configurations show the variety of microstructures achieved after coarsening with different infiltration loadings. Subfigures feature loadings of (a) 2%, (b) 4%, (c) 7%, (d) 9%, (e) 11%, (f) 14%, (g) 18%, and (h) 21%.

extended coarsening, the infiltrate has coarsened into a connected network of large clusters.

The dewetting process of a thin film on a planar substrate is generally considered to contain multiple stages such as hole formation, growth, and impingement. Furthermore, as material accumulates at the edge of the retracting film, in-plane instabilities may form finger-like patterns of ligaments that ultimately split into particle islands [25]. We expect that the active phase layer in these supported catalysts undergoes many of these processes during dewetting. Indeed, a more detailed analysis carried out in Sec. 3 demonstrates this for large infiltration loadings. For smaller loadings ($\lesssim$10%), on the other hand, the initial film thickness is less than the interface width. Dewetting behavior in this case is effectively driven by a long-range interaction (extending up to the scale of the interface width) between the droplets and the substrate until a dispersion of sufficiently resolved, bulk-like particles is formed. Such as-formed dispersions are qualitatively similar to what one would expect from the precipitation and deposition process that occurs from drying a precursor solution.

For the purpose of evaluating the evolution of performance-critical metrics, datasets are obtained for four randomly generated scaffolds, each tested with eight infiltration loadings. Fig. 4(a–d) show the evolution of the triple phase boundary (TPB) density. When plotted against infiltration loading, the total TPB initially reveals a maximum at low loading due to rapid dewetting and a dense population of small particles, as shown in Fig. 4(a). At higher infiltration loadings, the density is initially zero as instabilities in the film thickness have not yet merged with the support surface. As dewetting continues [Fig. 4(b)], the maximum TPB is reduced, and the TPB density at higher loadings increases as holes form in the film. These results during early stage dewetting are in qualitative accordance with other numerical studies that also report a maximum TPB at lower infiltration loadings followed by a gradual decline in TPB as the loading is increased (see Ref. [12], for example). These results also confirm the boost in TPB that can be obtained for nano-structured anodes, especially at metal volume fractions much lower than conventional values. However, as evolution progresses, the maximum TPB density continually falls closer to values typically associated with conventional cells. Meanwhile, the TPB density at intermediate and higher loadings tends to level around 2 μm^{-2} [Fig. 4(c)]. By the final configuration [Fig. 4(d)], the gap separating the maximum and minimum TPB densities has diminished to around 50%.

Another important consideration is the evolution of phase contiguity, a measure of connectedness or percolation degree of the active phase. Changes in contiguity can be caused by cluster splitting or merging events and render initially well-connected networks (contiguity of 1) completely non-conductive (contiguity of 0). These results are shown in Fig. 4(e–h). Sudden transitions in the contiguity result from dramatic variations between the sampled systems, as indicated by the error bars. For a loading of 10% or less, the infiltrate layer immediately forms isolated particles and the contiguity drops to zero. At loadings 14% and 18%, the systems maintain contiguity for some time before the connected ligaments and clusters separate into isolated parts. At 21%, the system maintains contiguity, but still shows some instability towards the end of the simulation, highlighting the deleterious effects of ongoing kinetic processes.

The total TPB and contiguity are synthesized in the form of the active TPB, which accounts only for the TPB generated by a contiguous network of the catalyst. This is shown alongside the total TPB in Fig. 4(a–d). For SOFC anodes, the preferable active phase loading will depend on the cell design. For ceramic scaffolds with negligible electronic conductivity, where the infiltrated phase must be a contiguous electronic conductor, our results suggest that a loading of at least 21% should be used to ensure stability. On the other hand, for MIEC scaffold materials, the infiltrate phase serves only as a catalyst, and the total TPB is of primary interest. In this case, the isolated particle microstructure observed near 4–7% loading maximizes the total TPB density, even after significant coarsening.

Referring back to Fig. 4(a–d), the TPB density at the lower infiltration loadings, namely 4–7%, experiences a steady reduction in value throughout the simulation. This is a bit perplexing considering that the film quickly dewetts the support surface to form particle islands and that the infiltrate mobility is limited to

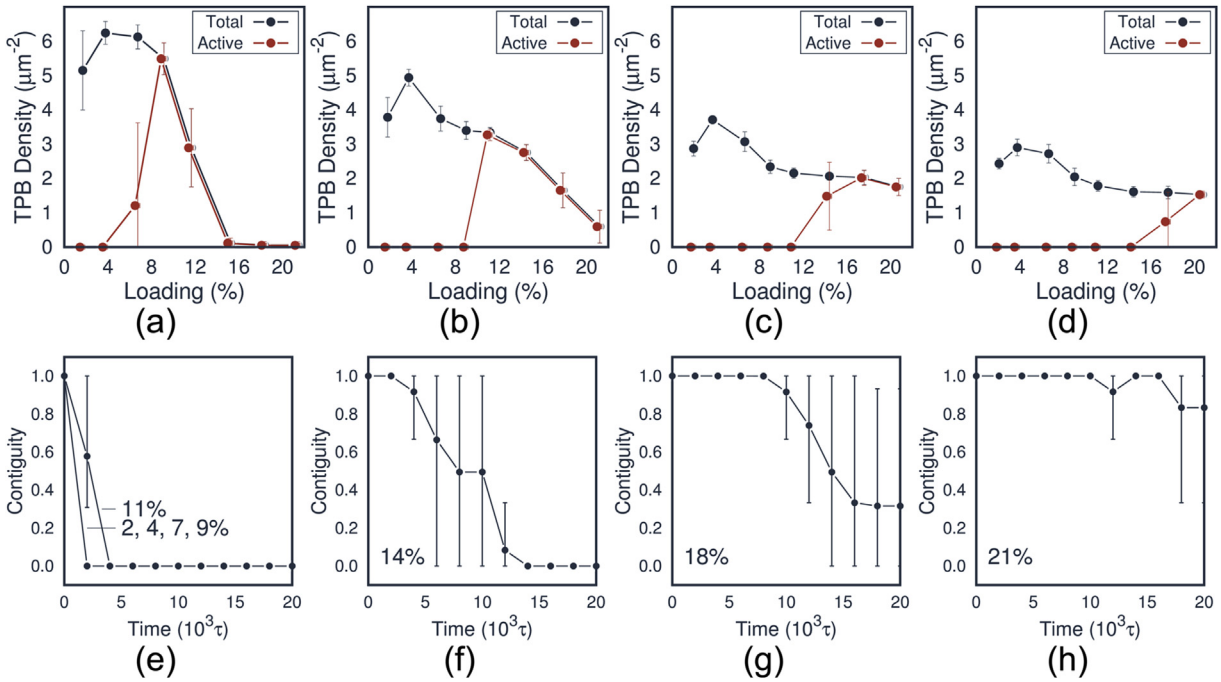

Fig. 4. Data obtained from 4 randomly generated scaffolds reveals degradation during active phase evolution. The total TPB density (black) and active TPB (red) are shown for simulation times (a) 400, (b) 2000, (c) 8000, and (d) 20000τ. Subfigures (e–h) show the contiguity for the infiltration loadings indicated on the panel. (For interpretation of the references to colour in this figure legend, the reader is referred to the web version of this article.)

particle interfaces. One might expect isolated particles to become kinetically trapped, essentially constraining the system to an energetically frustrated microstructure. However, visual inspection reveals that particles remain active throughout the simulation by sliding across the scaffold surface, sometimes colliding with nearby particles. Other particles can be seen shrinking until they disappear, apparently feeding into neighbor particles. An animation of the simulation included in the Supplemental Material displays many of these events. During the initial stage of the simulation, small particles quickly form and undergo a rapid reorganization. As the simulation continues, these processes become slower but continue to affect the particle dispersion.

The reorganization processes observed here for low catalyst loading are collectively referred to as particle sintering and can be explained using two mechanisms: Ostwald ripening (OR) and particle migration (PM) [27]. Both processes are observed experimentally and are common afflictions to catalytic system optimization. Hansen et al. suggest [27] that an ultra-thin layer of the catalyst is present on the support surface and mediates the material flux between otherwise isolated particles. This adlayer acts as a two-dimensional matrix phase, in analogy with traditional Ostwald ripening, and causes large particles to grow at the expense of small ones. It is also proposed that the material diffusion causes nanoparticle migration and possible coalesce as adatoms attach at one side of the particle and depart from the other. Despite a long history and intense research, there is an ongoing discussion concerning the exact nature of these mechanisms and the relative contribution of each to particle sintering. One method of identifying dominant mechanisms is to determine the kinetic exponent characteristic of power-law behavior. Theoretical models suggest that a growth law of the form $D^n - D_0^n = Ct$ can be used to fit the OR process with $n = \{3, 4\}$ or PM processes with $n = 7$ or greater [28]. Another proposed method involves characterizing the particle size distribution as being skewed-right (OR) or skewed-left (PM) [27,29].

Particle sintering is a primary culprit for thermal deactivation and warrants close examination here. The infiltrate order parameter, which generally assumes a value near zero far from the bulk, is observed to maintain values near 0.05 along the support surface even in the absence of infiltrate particles. While this value cannot be interpreted as a concentration, it does represent the presence of infiltrate material adsorbed on the surface and plays the role of an "ultra-thin layer." The infiltrate mobility present in the ultrathin layer is found to be near $M = 0.001$, three orders of magnitude less than its value at the particle surface ($M = 1$). Although the relative mobility is minuscule, it appears to play a significant role during extended evolution of the system as evidenced by particle migration and ripening. Representative examples of these mechanisms were selected from simulation results and are shown in Fig. 5 as two-dimensional slices through the evolving particles. The initial configurations, traced using the dashed lines, are superimposed with a time sequence of particle contours to capture both ripening [Fig. 5(a)] and migration/coalescence [Fig. 5(b)] processes. In OR, the smaller particle disappears without directly contacting the larger particle. In PM, one particle migrates a distance nearly equal to its radius before merging with a nearby particle of similar size. Fig. 5(c) shows the particle size distribution (PSD) for infiltration loading 2% at early (blue) and final (red) times. Drawing conclusions about dominant mechanisms from the PSD is notoriously delicate and requires ample sampling statistics with careful fitting. However, we note that a subtle bimodality appears to develop in the distribution suggesting that strong interactions with the heterogenous support plays a role in trapping some fraction of catalyst particles [29]. A log-log plot of the average effective particle diameter ($D_{eff} = (6V/\pi)^{(1/3)}$) reveals interesting scaling behavior at extended timescales. The solid lines are plotted for a growth exponent $n \simeq 7$ and the growth coefficient is chosen to fit the data. According to the analysis carried out in Ref. [28], this scaling indicates that particle migration is a dominant mechanism in the evolution of the active phase at lower infiltration loadings. Higher infiltration loadings (7 and 9%) display slower particle size

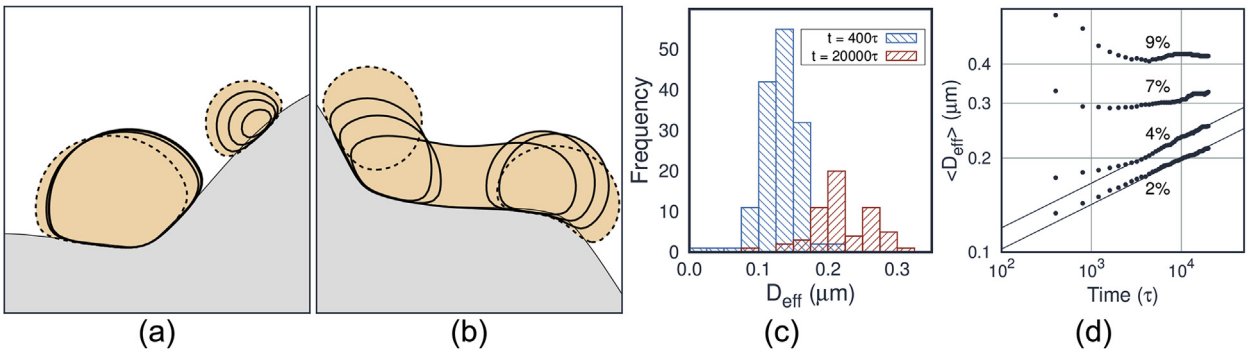

Fig. 5. Ostwald ripening and particle migration lead to significant evolution in particle dispersions. Representative cases of Ostwald ripening (a) and particle migration (b) are selected from simulation and displayed with overlapping sequences of interface contours. The initial configuration is signified by a dashed contour. Early and final stage particle size distributions are shown in (c) to illustrate the agglomerative effects of these kinetics processes. In subfigure (d), the average effective particle diameter measured from simulation results (filled circles) is compared to a power-law fit (solid line) with growth exponent $n = 7$.

evolution. This is likely due to increased interaction with the heterogeneous support as particles become larger.

3.2. Effects of scaffold structures

For the results presented previously, the scaffold is generated using a procedure designed to mimic the acid leaching process. We now construct a different scaffold designed to mimic the pyrolysis of pore-forming particles and perform a comparison. The objective is to determine if the morphological features of the scaffold play a significant role in infiltrate coarsening and identify if one fabrication process may be preferable. A more detailed introduction to these techniques and the scaffold construction was provided in Sec. 2.

Fig. 6 (a) and (e) display SEM images (reproduced with permission and adapted for this work) of scaffolds produced by acid leaching [30] and pyrolysis [31] of the pore-former material, respectively. Note that the leached scaffold features highly faceted particle faces with relatively sharp edges while the pyrolyzed scaffold features more rounded particles that create a sponge-like nature. These differences can be reasonably explained in terms of sintering conditions. Whereas the leached scaffold contains pore-former particles throughout sintering, the pyrolyzed scaffold removes them early in the sintering process. Simple modifications in our scaffold construction process can capture the dominant microstructural features and exemplify those observed experimentally. Fig. 6(b) and (f) display the numerical scaffolds with their surfaces colored by local mean curvature. The leached scaffold features flat faces outlined with high curvature grain boundary edges. The pyrolyzed scaffold exhibits low curvature bulbs joined at high curvature necking regions. The surface curvatures are mapped onto a plane spanned by the principal curvatures in Fig. 6(c) and (g) to more quantitatively identify dominant microstructural features. The high density areas extending along the vertical and horizontal axis in Fig. 6(c) represent the many concave and convex scaffold edges. In Fig. 6(g), the negative curvature of the sintered necks dominates, and the peak density is slightly offset from the origin due to nearly spherical surfaces. As another potential application of this analysis, curvature densities could be compared to experimental tomographic data to more quantitatively verify a faithful, numerical representation of the scaffold.

Despite the marked differences in scaffold microstructure between the two preparation procedures, only slight deviations can be seen in the infiltrate evolution. Fig. 6(d) and (h) show the final configuration for each scaffold with a 2% infiltration loading. In both systems, the catalyst particles tend to agglomerate along the boundaries between grains where the scaffold curvature is greatest. However, the pyrolysis scaffold [Fig. 6(h)] features a slightly higher particle number density of the active phase. This might be attributed, in part, to the enhanced curvature of the necking regions between the rounded particles, which seem to act as effective particle trapping regions. It is possible that the extreme geometric heterogeneity of the scaffold geometry offers a low energy configuration for particles, reduces the driving force for further evolution, and slows the kinetic processes. TPB densities are displayed in Fig. 7(a) for the scaffolds representing the acid leaching (black) and pyrolysis (red) procedures. The pyrolyzed scaffold exhibits slightly enhanced TPB density, especially at lower infiltration loadings. A more detailed analysis following this line of inquiry on particle trapping may be beneficial in identifying features that can be exploited to stabilize particle dispersions.

3.3. Effects of contact angle

In all of the results presented thus far, the interaction between the support and infiltrate is constant. We now explore the effect of this interaction by considering multiple contact angles, $\theta_c = 60°, 90°, 120°$. The phase field model is developed to allow the contact angle to be set directly from model parameters (details can be found in Sec. 2.1). Simulations were carried out once more on the scaffold prepared by leaching pore-forming particles. An immediate observation from the coarsened systems (not shown here) is that lower contact angles result in larger particle sizes and a reduced particle number density. Visual inspection reveals limited particle mobility with only very close neighbors coagulating into larger particles.

Fig. 7(b) displays the final TPB density curves for three contact angles. We do not observe any significant trends in the rate of TPB reduction during particle sintering. This is in contrast with the results of the kinetic Monte Carlo study presented in Ref. [15] where the lower contact angle hastens TPB reduction. This is likely due, in part, to differences in the initial conditions. In the cited work, a monodisperse particle distribution is assumed initially, whereas the particles in the present work form from a dewetting process. The early-stage microstructure for $\theta_c = 60°$ is remarkably different from that of $\theta_c = 120°$. Despite the observable differences in the microstructure, the TPB densities approach similar values during coarsening. It appears that the reduced particle number density of lower contact angles is offset, somewhat, by smaller particle height and increased wetting area.

As the thickness of the infiltrate layer is increased and the contact angle is decreased, the driving force for hole formation and

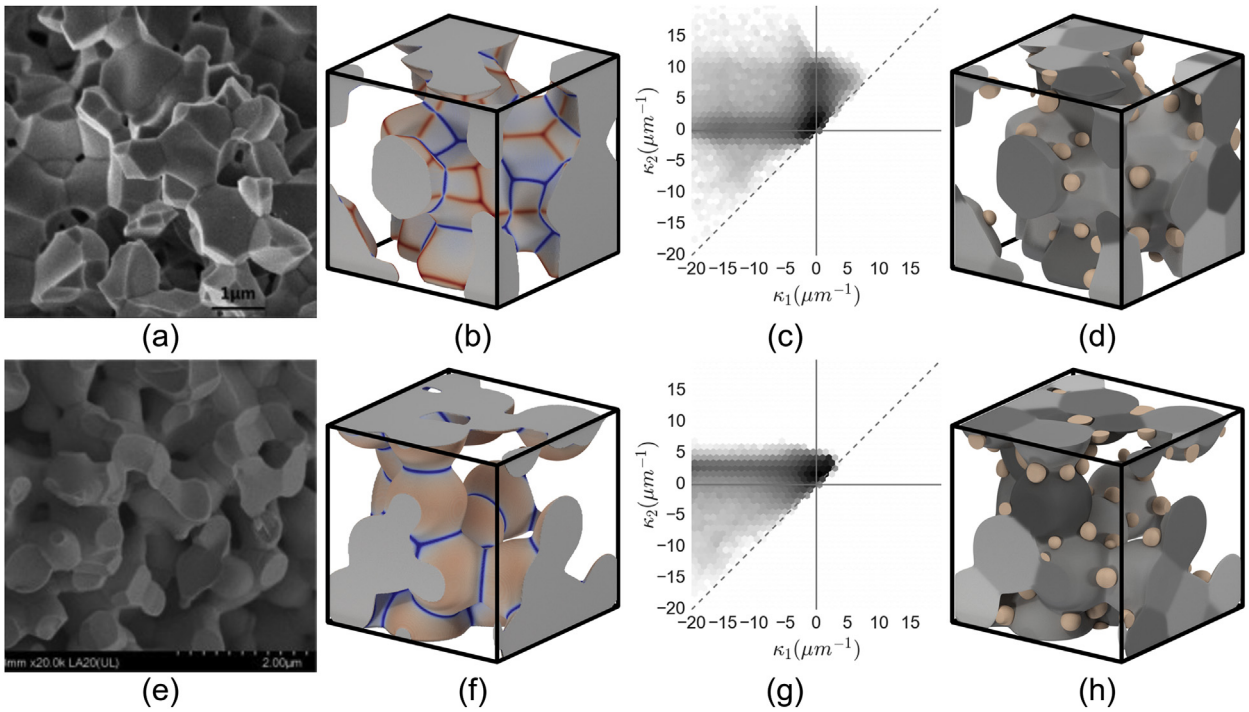

Fig. 6. A side-by-side comparison of experimental and numerical scaffolds reveals strikingly different geometric features. Scaffolds produced using (a) acid leaching [30] and (d) pyrolysis [31] are compared to their numerical counterparts shown in (b) and (f), where the surfaces are colored by local mean curvature. Subfigures (c) and (g) show the corresponding principal curvature density plots using a logarithmic scale for intensity. The final configurations ($t = 20000\tau$) are displayed for each scaffold in (d) and (h) for an infiltration loading of 2%.

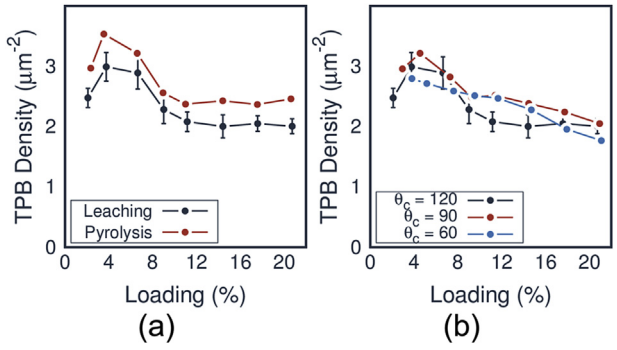

Fig. 7. Scaffold morphology and active phase wettability are tested for their effect on the evolution of the active phase. Subfigures show the total TPB measured from simulations with (a) different scaffold construction techniques and (b) multiple infiltrate-scaffold contact angles.

growth is reduced. During the time required for hole formation, commonly referred to as the induction period [25], the film completely covers the scaffold surface, and the TPB density is zero. As holes nucleate and the film recedes, the TPB increases rapidly. Fig. 8(a) shows a cross-sectional slice through the film as its contour evolves during hole formation and growth. It appears that holes tend to form at the corners of scaffold particles and the film edges recede until the holes impinge. Jiran and Thompson formulate the rate of growth of the dewetted area on a planar substrate [32]. Their model proposes that as displaced material builds up around the rim, the hole perimeter forms instabilities that protrude into the film and grow at a constant rate given as $\bar{r} = 2D_s\Omega^2\gamma_s/\pi kTh^3$. Note that the growth rate of the dewetted area depends inversely on the third power of the film thickness. Roughly speaking, a thicker film results in more displaced material, less curvature to drive growth, and longer diffusion pathways. In a follow up study, they employ these findings in an Avrami-type nucleation and growth analysis of the agglomerated area [33]. A similar approach is used here to formulate the TPB as the edge of dewetted regions, $TPB = N_h(2\pi\bar{r}(t-\xi))$, where ξ is the incubation period and N_h is the number of holes. Employing the growth rate from above yields $TPB \sim N_h\gamma_s(t-\xi)/h^3$. This assumes that holes form simultaneously and that the number of holes N_h depends only weakly on the film thickness. Our observations indicate that assuming simultaneous hole nucleation is reasonable given the strong, geometric heterogeneity of the support and its tendency to promote hole formation. While these assumptions are certainly debatable, the initial incline in TPB does appear to scale with $1/h^3$ as indicated in Fig. 8(b). The solid lines are fitted to intercept the time axis at the appropriate incubation period, and the inclination is adjusted using the film thickness, h, for each infiltration loading and scaling the slope by $1/h^3$. Fig. 8(c) shows the same data where curves of rescaled TPB collapse onto each other, highlighting the expected scaling behavior at early times.

4. Discussion

A recurring theme throughout the previous section is that kinetic processes conspire to bring about thermal deactivation. The infiltration technique is often purported as an antidote to the ailments exhibited by conventional SOFCs, and yet it suffers from similar symptoms. Although the initial dewetting stage of infiltrated systems produces favorable structures, extended coarsening processes resulted in large clusters and TPB densities comparable to conventional cells. Likewise, phase contiguity was only maintained for relatively high infiltration loadings.

These results reinforce the need for modifications designed to arrest or significantly slow the Rayleigh splitting, particle

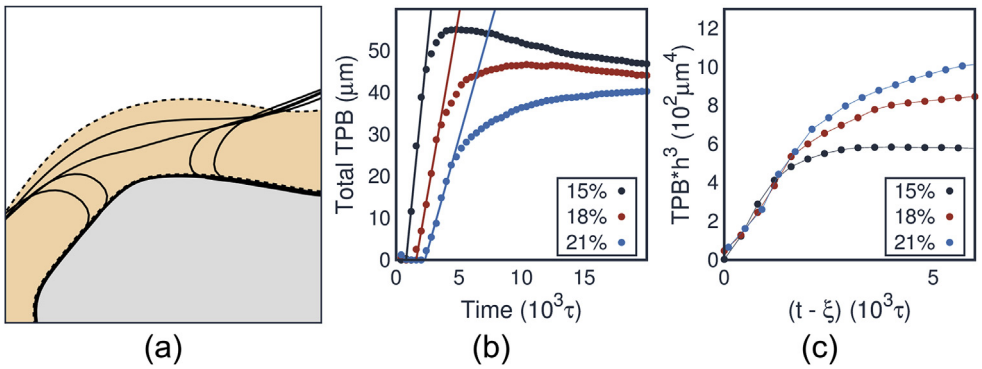

Fig. 8. Active phase evolution at early times for infiltration loadings of 15, 18, and 21% are described using the kinetics of film dewetting. (a) A profile view of the active phase (orange) and scaffold (grey) indicates the formation and growth of holes using a sequence of interface contours. (b) The initial increase in the total TPB scales inversely with the cube of film thickness. After rescaling the TPB and accounting for the incubation period (c), the curves collapse during hole growth. (For interpretation of the references to colour in this figure legend, the reader is referred to the web version of this article.)

migration, and ripening that lead to thermal deactivation. Our simulations suggest that heterogeneity in the scaffold geometry can affect infiltrate evolution. This effect is seen when small particles become trapped in necking regions between scaffold particles, effectively slowing the kinetic processes. Unfortunately, these features led to only a slight enhancement in TPB density. However, more extreme approaches to intensify scaffold heterogeneity have proven beneficial experimentally. For example, dual phase infiltration can be used to infiltrate the scaffold material into the sintered scaffold to produce nano-scale texture onto the scaffold surface, before infiltrating the catalyst. Another approach is to treat the scaffold with acid to etch small scale features into the microstructure [34]. Such innovations in microstructural engineering are necessary to ensure stability.

The phase field method has been demonstrated here as a useful tool to study infiltrated systems and is capable of capturing the kinetic processes that occur during dewetting and agglomeration. Furthermore, the accuracy of the diffuse interface approach is firmly established in the sharp interface limit, where a connection can be made between the diffuse interface model and a corresponding sharp interface description of a moving boundary problem [35]. However, the spatial resolution of the computational grid required to resolve the diffuse interface is a significant limitation. This is especially challenging in supported metal catalyst systems due to the disparity in length scales between the fine structure of the infiltrated material and the large scaffold particles. The difference in length scales is a key factor in the favorable properties of these systems, and it is critical that direct, numerical simulations feature sufficient resolution to capture the spectrum of structure sizes. In this study, with the aid of distributed memory parallelization, we have found that a grid size of 180^3 points strikes a suitable balance between resolving fine structures and accessing the time scales of interest. Unfortunately, this resolution is not amenable to the thin infiltrate layers that form the initial conditions in systems with low infiltration loadings. In this case, the thickness of the infiltrate layer is only a few grid cells, which is not thick enough to feature bulk and interface components. Furthermore, the physical description of such thin layers may feature long-range surface interactions with the support structure, making the appropriate sharp interface description unclear. The applicability of this model with the chosen resolution only strictly holds in the case where such thin layers in low loading systems have coarsened into particles whose linear dimension is large relative to the interface width. For our purposes, it is sufficient to limit our attention to the simulation following the initial dewetting and take the early particle dispersion as the initial conditions. Fortunately, these initial particle dispersions are reasonable approximations to the small islands that are expected to form during typical fabrication processes.

Aside from the ability to numerically resolve fine structures, there is some flexibility in setting the catalyst's initial configuration. This is attributed to the multiplicity of methods for fabricating supported catalysts and subtle variations in treatment steps including drying, calcining, and reduction. Details of preparation intermediates and the initial metal dispersion will certainly depend significantly on processing conditions. For example, notable changes in catalyst microstructure have been demonstrated by skipping calcination [36], using urea or other additives, and dual-infiltration [37]. Some numerical studies have assumed a monodisperse particle layer where the particle radius is informed from experimental studies, as in Ref. [12] for example. In the work presented here, the active phase initially forms a uniform layer on the support. One advantage to this approach is that the metal dispersion forms naturally from the agglomeration process. However, for very low infiltration loadings, it is more likely that the metal precursor deposits as particle islands or nucleates as clusters on the support. In any case, these assumptions are an idealization of a complex process and may be relieved with detailed statistics or experimental data to construct initial conditions targeted to a specific system.

A few additional points that warrant mention concern the crystallinity of the infiltrate phase. We approximate it to be monocrystalline, despite certain polycrystallinity of the infiltrated particle layer. This is significant because film instabilities are known to form from grain boundary grooving and could be critical in setting the characteristic size of a dewetting layer [25]. While the sintering model used here is capable of handling a large number of grains, the computational cost of a polycrystalline representation is prohibitive and severely limits accessible simulation timescales at present time. On a related note, we assume an isotropic surface energy for the infiltrate phase. This will deviate most notably from the physical system for low-temperature operation since faceting is believed to slow the kinetics of particle migration [28].

5. Conclusion

We have developed and employed a numerical approach to craft realistic metal supported catalyst structures and provide insight into their evolution. A multistep process was used to construct scaffolds with morphological characteristics comparable to experimental reports, and infiltration of an active catalyst phase was approximated as a uniform layer applied to the support surface.

Evolution of the active phase driven by a reduction in the total interface energy was simulated using a phase field model to capture the dewetting, particle agglomeration, and coarsening that take place during extended operation at elevated temperatures. Low infiltration loadings (< 7%) rapidly developed a dispersion of small particles and continued coarsening. We attribute the deactivation to the well-known mechanisms of Ostwald ripening and particle migration. A quantitative analysis of the particle size evolution reveals an apparent power law scaling behavior at late times with growth exponent $n \simeq 7$, consistent with kinetics dominated by particle migration. Moderate loadings (7–15%) briefly exhibited a semi-continuous network of ligaments that break up through Rayleigh-type instabilities and further coarsen into large clusters. The infiltration loading greater than 20% maintained contiguous networks during the timescale of interest.

During early stage dewetting, the measured triple phase boundary (TPB) revealed a familiar curve that features a maximum at low infiltration loading, agreeing qualitatively with other studies. However, extended evolution resulted in a severe reduction in the TPB density. The maximum TPB occurs at an active phase loading around 4–7% and degrades over 60% during the course of the simulation. A percolation threshold near 20% was clearly identified as the loading required to maintain stability of an electronically conductive network over the simulated timescales (approximately 10 h).

We also investigated the performance of pyrolysis versus acid leaching pore-forming techniques, and the effects of scaffold morphology on active phase coarsening. The pyrolyzed scaffold showed slightly enhanced total TPB, indicating that strong heterogeneity in the scaffold geometry may induce a particle trapping effect. Modification of the metal catalyst-support interaction, as measured by the contact angle, showed remarkably little effect on the TPB density after coarsening, despite notable differences in the infiltrate microstructure. Thus, this work suggests that neither modifications in the large scale structure of the scaffold nor fine-tuning the metal catalyst-support interaction will significantly affect important microstructural metrics associated with the performance of SOFC anodes. We speculate that such improvements may be possible, on the other hand, by patterning the scaffold surfaces at the nanoscale so as to kinematically trap a dispersion of droplets at imperfections (such as surface ridges and troughs).

Acknowledgements

Funding for this research has been provided by Princeton University. We gratefully acknowledge the High Performance Computing Research Center at Princeton University for providing the computational resources for the project.

Appendix A. Supplementary data

Supplementary data related to this article can be found at https://doi.org/10.1016/j.jpowsour.2017.09.066.

References

[1] H. Knözinger, K. Kochloefl, Ullmann's Encyclopedia of Industrial Chemistry, vol. 1, Wiley-VCH Verlag GmbH & Co. KGaA, Weinheim, Germany, 2000.
[2] Z. Liu, B. Liu, D. Ding, M. Liu, F. Chen, C. Xia, Fabrication and modification of solid oxide fuel cell anodes via wet impregnation/infiltration technique, J. Power Sources 237 (2013) 243–259.
[3] S.P. Jiang, Nanoscale and nano-structured electrodes of solid oxide fuel cells by infiltration: advances and challenges, Int. J. Hydrogen Energy 37 (1) (2012) 449–470.
[4] J.T.S. Irvine, D. Neagu, M.C. Verbraeken, C. Chatzichristodoulou, C. Graves, M.B. Mogensen, Evolution of the electrochemical interface in high-temperature fuel cells and electrolysers, Nat. Energy 1 (1) (2016) 15014.
[5] R. Gorte, J. Vohs, Nanostructured anodes for solid oxide fuel cells, Curr. Opin. Colloid Interface Sci. 14 (4) (2009) 236–244.
[6] P. Keyvanfar, V. Birss, Optimization of infiltration techniques used to construct Ni/YSZ anodes, J. Electrochem. Soc. 161 (5) (2014) F660–F667.
[7] T. Klemensø, K. Thydén, M. Chen, H.-J. Wang, Stability of Ni–yttria stabilized zirconia anodes based on Ni-impregnation, J. Power Sources 195 (21) (2010) 7295–7301.
[8] A.N. Busawon, D. Sarantaridis, A. Atkinson, Ni infiltration as a possible solution to the redox problem of SOFC anodes, Electrochem. Solid-State Lett. 11 (10) (2008) B186–B189.
[9] M. Lomberg, E. Ruiz-Trejo, G. Offer, N.P. Brandon, Characterization of Ni-Infiltrated GDC electrodes for solid oxide cell applications, J. Electrochem. Soc. 161 (9) (2014) F899–F905.
[10] M. Kishimoto, M. Lomberg, E. Ruiz-Trejo, N.P. Brandon, Enhanced triple-phase boundary density in infiltrated electrodes for solid oxide fuel cells demonstrated by high-resolution tomography, J. Power Sources 266 (2014) 291–295.
[11] E. Hardjo, D.S. Monder, K. Karan, Numerical modeling of nickel-impregnated porous YSZ-supported anodes and comparison to conventional composite Ni-YSZ electrodes, ECS Trans. 35 (2011) 1823–1832.
[12] Y. Zhang, Q. Sun, C. Xia, M. Ni, Geometric properties of nanostructured solid oxide fuel cell electrodes, J. Electrochem. Soc. 160 (3) (2013) F278–F289.
[13] A.J. Reszka, R.C. Snyder, M.D. Gross, Insights into the design of SOFC infiltrated electrodes with optimized active TPB density via mechanistic modeling, J. Electrochem. Soc. 161 (12) (2014) F1176–F1183.
[14] A. Bertei, J.G. Pharoah, D.A.W. Gawel, C. Nicolella, A particle-based model for effective properties in infiltrated solid oxide fuel cell electrodes, J. Electrochem. Soc. 161 (12) (2014) F1243–F1253.
[15] Y. Zhang, M. Ni, M. Yan, F. Chen, Thermal aging stability of infiltrated solid oxide fuel cell electrode microstructures: a three-dimensional kinetic Monte Carlo simulation, J. Power Sources 299 (2015) 578–586.
[16] L. Liang, Q. Li, J. Hu, S. Lee, K. Gerdes, L.-Q. Chen, Phase field modeling of microstructure evolution of electrocatalyst-infiltrated solid oxide fuel cell cathodes, J. Appl. Phys. 117 (6) (2015) 065105.
[17] L.-Q. Chen, Phase-field models for microstructure evolution, Annu. Rev. Mater. Res. 32 (1) (2002) 113–140.
[18] H.P. Bonzel, E.E. Latta, Surface self-diffusion on Ni(110): temperature dependence and directional anisotropy, Surf. Sci. 76 (2) (1978) 275–295.
[19] N. Moelans, B. Blanpain, P. Wollants, Quantitative analysis of grain boundary properties in a generalized phase field model for grain growth in anisotropic systems, Phys. Rev. B 78 (2) (2008) 024113.
[20] A. Tsoga, A. Naoumidis, P. Nikolopoulos, Wettability and interfacial reactions in the systems and Ni/Ti-TiO2/YSZ, Acta Mater 44 (9) (1996) 3679–3692.
[21] Akash M.J. Mayo, Zr surface diffusion in tetragonal yttria stabilized zirconia, J. Mater. Sci. 35 (2) (2000) 437–442.
[22] N. Provatas, K. Elder, Phase-field Methods in Materials Science and Engineering, first ed., Wiley-VCH, 2010.
[23] M. Skoge, A. Donev, F.H. Stillinger, S. Torquato, Packing hyperspheres in high-dimensional Euclidean spaces, Phys. Rev. E 74 (4) (2006) 041127.
[24] C. Rycroft, Voro++: a Three-dimensional Voronoi Cell library in C++, Lawrence Berkeley National Laboratory.
[25] C.V. Thompson, Solid-state dewetting of thin films, Annu. Rev. Mater. Res. 42 (1) (2012) 399–434.
[26] M.S. McCallum, P.W. Voorhees, M.J. Miksis, S.H. Davis, H. Wong, Capillary instabilities in solid thin films: lines, J. Appl. Phys. 79 (10) (1996) 7604–7611.
[27] T.W. Hansen, A.T. DeLaRiva, S.R. Challa, A.K. Datye, Sintering of catalytic nanoparticles: particle migration or Ostwald ripening? Acc. Chem. Res. 46 (8) (2013) 1720–1730.
[28] P.J.F. Harris, Growth and structure of supported metal catalyst particles, Int. Mater. Rev. 40 (3) (1995) 97–115.
[29] P. Tabib Zadeh Adibi, V.P. Zhdanov, C. Langhammer, H. Grönbeck, Transient bimodal particle size distributions during Pt sintering on alumina and Silica, J. Phys. Chem. C 119 (2) (2015) 989–996.
[30] J. Ju, J. Lin, Y. Wang, Y. Zhang, C. Xia, Electrical performance of nanostructured strontium-doped lanthanum manganite impregnated onto yttria-stabilized zirconia backbone, J. Power Sources 302 (2016) 298–307.
[31] M. Liu, S. Wang, T. Chen, C. Yuan, Y. Zhou, S. Wang, J. Huang, Performance of the nano-structured Cu–Ni (alloy) -CeO2 anode for solid oxide fuel cells, J. Power Sources 274 (2015) 730–735.
[32] E. Jiran, C.V. Thompson, Capillary instabilities in thin films, J. Electron. Mater 19 (11) (1990) 1153–1160.
[33] E. Jiran, C.V. Thompson, Capillary instabilities in thin, continuous films, Thin Solid Films 208 (1) (1992) 23–28.
[34] R. Küngas, J.-S. Kim, J.M. Vohs, R.J. Gorte, Restructuring porous YSZ by treatment in hydrofluoric acid for use in SOFC cathodes, J. Am. Ceram. Soc. 94 (7) (2011) 2220–2224.
[35] K.R. Elder, M. Grant, N. Provatas, J.M. Kosterlitz, Sharp interface limits of phase-field models, Phys. Rev. E 64 (2) (2001) 021604.
[36] H. He, J.M. Vohs, R.J. Gorte, Effect of Synthesis conditions on the performance of Cu CeO2 YSZ anodes in SOFCs, J. Electrochem. Soc. 150 (11) (2003) A1470–A1475.
[37] S. Jung, C. Lu, H. He, K. Ahn, R.J. Gorte, J.M. Vohs, Influence of composition and Cu impregnation method on the performance of Cu/CeO2/YSZ SOFC anodes, J. Power Sources 154 (1) (2006) 42–50.